SAND2019-4758C

Spark Assisted Compression Ignition Engine with Stratified Charge Combustion and Ozone Addition

Author, co-author (Do NOT enter this information. It will be pulled from participant tab in MyTechZone)

Affiliation (Do NOT enter this information. It will be pulled from participant tab in MyTechZone)

Abstract

Performance and emissions characteristics for stratified charge spark assisted compression ignition (SACI) with 30 ppm of added ozone (O_3) were explored in a single-cylinder, optically accessible, spray-guided, research engine. For the present study, intake pressure and temperature were fixed at 1.0 bar and 42°C respectively, with a range of engine loads (1.5 – 5.5 bar indicated mean effective pressure) and speeds (800 – 1600 revolutions per minute) explored. Fuel stratification – achieved by a late-cycle injection of ~ 10-25% of the total fuel – was used to maintain stable operation at lower engine loads. For each condition spark timing, second injection SOI, and fuel split ratio between the main and second injection were optimized to maximize engine performance while maintaining nitrogen oxide emissions (NOx) below 5 g/kg-fuel.

Ozone addition was found to decrease specific fuel consumption by up to 9%, with across the board improvement in combustion stability relative to similar conditions without O_3. The effect of O_3 addition was most substantial for the lowest loads. Moreover, because a higher fraction of the fuel burned was due to end-gas auto-ignition, specific NOx emissions likewise decreased by up to 30%. From complementary measurements of in-cylinder O_3 decomposition acquired via an ultraviolet light absorption diagnostic, it was observed that rapid decomposition of O_3 into molecular and atomic oxygen coincided with the onset of end-gas auto-ignition. The burst of resultant atomic oxygen was thought to accelerate low-temperature heat release (LTHR) reactions in the end gas. Optimal end-gas auto-ignition started between 20 and 30 crank angles before top dead center with temperatures at LTHR onset estimated to be between 575 and 700 K. An included analysis indicates that the spark deflagration was needed to add between 10 and 40 J of additional thermal energy to the end gas to achieve optimal auto-ignition.

Introduction

Current automotive gasoline engine research trends are focused on combustion modes that use some amount of bulk-gas auto-ignition. Until recently, most investigations were into advanced compression ignition (ACI) concepts that exclusively feature auto-ignition such as gasoline compression ignition (GCI) [1-3] or homogeneous charge compression ignition (HCCI) [4, 5]. Relative to conventional spark ignited (SI) combustion, these low-temperature combustion (LTC) strategies achieve substantially improved fuel economy and much lower engine-out emissions of nitrogen oxides (NOx) and particulate matter (PM) through a combination of reduced throttling losses, lower heat transfer, higher compression ratios, and increased charge specific heat ratios.

The central challenge for ACI implementation has been to maintain stable and knock-free combustion across the load-speed map. At lower loads where combustion stability is problematic, charge heating via retained residuals along with mixture preparation from late-cycle direct injections and internal flows are often used to create reactive, heterogeneous mixtures at top dead center (TDC) [1, 6-8]. However, the improved stability comes at the cost of increased heat transfer losses [9] and more complex valve train requirements. For elevated loads, engine knock can be mitigated with substantial dilution by cooled exhaust gas recirculation (EGR) to slow heat release rates [10, 11], but requires extensive intake boost to meet power density requirements. As a result, expansion efficiency is reduced, and mechanical losses are increased due to the higher peak cylinder pressure requirements.

An alternative to ACI engine combustion is the so-called mixed-mode combustion strategy, where some combination of spark-assisted compression ignition (SACI) and pure ACI are used at part-load operation with exclusive SI combustion used for high power-density conditions [12, 13]. For the SACI strategy, end-gas auto-ignition is induced by compression heating from an expanding spark initiated flame kernel [14-23]. Compression ratios must generally be held to below 14 to limit high-load knock, which is much lower than the 16+ compression ratios commonly used for conventional ACI. As a result, some combination of mixture stratification and charge heating at intake valve closure (IVC) is once again required to ensure that gasoline mixtures near TDC are sufficiently reactive.

Another potential method to improve charge reactivity is to seed the intake charge with small amounts ($\sim 10 - 70\ ppm$) of ozone (O_3) – a powerful oxidizing chemical agent. Ozone addition enhances the reactivity of gasoline-like fuels, which thereby enables stable auto-ignition with less initial charge heating [2, 24-29]. Because charge reactivity is proportional to the initial O_3 concentration and targeted O_3 concentrations can be generated by onboard coronal discharges of intake air [30], the engine transient response can be very high. The authors previously demonstrated that 50 ppm of intake added O_3 for homogeneous charge SACI operation led to excellent combustion performance for moderate loads and NOx emissions below 1 g/kg-fuel [29]. However, poor combustion stability prevented operation at loads below ~4 bar indicated mean effective pressure (IMEP).

Ozone addition works by effectively acting as an atomic oxygen (O) carrier that is rapidly released near TDC when temperatures reach around 600 K. The newly formed O then initiates heat release through fuel hydrogen (H) abstraction to form fuel (R) and hydroxyl (OH) radicals [28, 31]. The OH likewise abstracts additional H to make additional R. For temperatures below ~800 K, chain branched low-temperature heat release (LTHR) pathways dominate. For these reactions, R combines with molecular oxygen (O_2) to form peroxy radicals (RO_2). The RO_2 continues fuel H abstraction through the reaction: $RO_2 + RH \rightarrow ROOH + R$, with the formed fuel radical peroxide (ROOH) decomposing into oxy radical (RO) and OH [32]. Depending on initial intake O_3 concentrations, these early LTHR reactions can advance combustion phasing by more than 20 crank angles (CA).

For the present study, the effect of intake seeded O_3 (30±4 ppm) was investigated as a way to replace charge pre-heating for stable lean SACI operation with an early and late direct injection (DI). Experiments were performed in a spray-guided single-cylinder research engine with optical access. A naturally aspirated intake pressure and 42°C intake temperature were maintained for all conditions, with internal residual fractions of between 10 and 18% achieved through a combination of positive valve overlap (PVO) and moderate exhaust backpressures. Low to moderate engine loads of between 1.5 and 5.5 bar indicated mean effective pressure (IMEP) and speeds of between 800 – 1600 revolutions per minute (rpm) were examined. Each load/speed operating condition was optimized to maximize engine performance while maintaining nitrogen oxide emissions (NOx) below 5 g/kg-fuel. For selected optimized operating points, the effect of four parameters were studied in detail: a) intake O_3 concentration, b) spark timing (ST), c) timing of the second injection with respect to ST, and d) the fuel split ratio between the main and second injections. Performance and engine-out emissions measurements were complemented by CA resolved O_3 measurements performed via ultraviolet (UV) light absorption. Finally, estimates of end gas auto-ignition onset and corresponding temperature are used to evaluate the amount of thermal energy required to initiate auto-ignition with O_3 addition.

Experimental Setup

Sandia Single-Cylinder Research Engine

All experiments were performed in a 4-valve, single-cylinder, spray-guided, research engine. The combustion chamber features opposed, wall-mounted circular quartz windows (12.7 mm clear aperture) that provide pent roof optical access. Fuel was injected via a centrally mounted Bosch step-hole (HDEV 1.2) injector with 8 uniformly distributed 125 µm diameter nozzles that form a 60° umbrella angle. Each cycle featured an early direct injection with a fixed start of injection (SOI) at -230 CA and a late second injection with the SOI timed just after ST. The second injection SOI was varied between -64 to -36 CA. Combustion for each cycle was initiated by an NGK long-reach resistor spark plug that was driven by a 93 mJ Bosch ignition coil. To better illustrate the injection and in-cylinder combustion processes, a schematic of the combustion chamber with the piston position near TDC is provided in Figure 1. Two of the fuel sprays straddle the spark plug gap with virtually all of the fuel spray for injections later than -80 CA entering the piston bowl. The initial deflagration is believed to be confined to the piston bowl where mixtures are fuel-rich. Compressive heating by the deflagration then leads the leaner end gas mixtures to transition to auto-ignition.

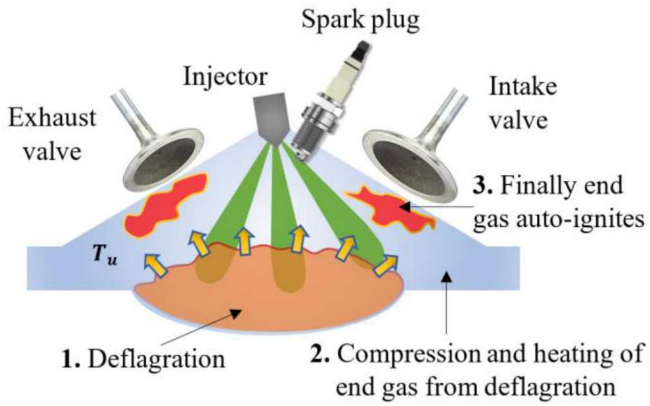

Figure 1. Schematic of the engine combustion chamber.

Intake and exhaust cams were set to create 34 CA of PVO centered at TDC. A motoring dynamometer was used to vary engine speeds between 800 and 1600 rpm. A BEI Sensors optical engine encoder with 0.1 CA resolution measured crank angle position. Intake runner and port designs limited swirl and tumble flows to minimize heat transfer losses from in-cylinder generated turbulence. An Aquatherm circulator heat exchanger maintained cylinder wall and head temperatures to a fixed 90°C. Because the optical piston was uncooled and the initial deflagration was in the piston bowl, it is likely that piston surface temperatures and heat transfer losses through the piston were much higher. A summary of relevant engine geometry details, valve, injection and spark timings, and operating characteristics is provided in Table 1.

Table 1. Engine specifications and operating conditions.

Displaced volume [cm^3]	551
Bore/Stroke/Connecting Rod [mm]	86 / 95.1 / 166.7
Geometric Compression Ratio	13:1
Intake Valve Open/Close [CA]†	343 / -145
Exhaust Valve Open/Close [CA]†	160 / -343
Valve Lift [mm]	9.7
Fuel Pressure [bar]	100
Injector Hole Number	8
Injector Cone Angle [°]	60
Injector Orifice Diameter [µm]	125
Intake/Exhaust Pressure [kPa]	100 / 105
Intake Temperature [°C]	42
Intake O_3 Concentration [ppm]	0 – 34
Engine Speed [rpm]	800, 1000, 1200, 1400, 1600
Cycle fueling rates [mg/cycle]	8.1 – 17.9
Charge mass equivalence ratio	0.27 – 0.56
Residual gas fraction [%]	10 – 18
Spark Timing	-70 – -28
Main SOI [CA]†	-230
2nd injection SOI [CA]	-64 – -36
2nd injection fueling fraction [%]	10 – 25

†0 CA corresponds to TDC of the compression stroke

Intake air was controlled by a Tescom ER5000 PID (Proportional, Integral, Derivative) pneumatic actuator that precisely regulates gas

supply pressures upstream of an orifice plate. Pressures and temperatures were measured in both the intake and exhaust runners, with wire-wrapped resistive heaters and fiberglass insulation in the exhaust runner used to minimize gas temperature changes from heat transfer. A Chromalox circulation heater positioned between the intake plenum and air supply line was used to heat the intake charge up to 42°C. Intake and exhaust pressures were fixed at 1.0 and 1.05 bar respectively, which with the use of PVO produced moderate residual gas fractions of between 10 and 18%. Because no external EGR was used, lean charge equivalence ratios (ϕ) of below 0.6 were maintained for all conditions examined here. Cylinder pressure was measured by a Kistler 6125A piezo-electric pressure sensor, with these data used to extract heat release and load data for each cycle. Ozone was seeded directly into the intake runner using an Ozone Solutions OZV-4 O_3 generator, with the O_3 concentration set by varying the amount of dry air through the generator using an MKS GE50 mass flow controller. The O_3 concentration out of the generator was directly measured via a Teledyne API 452 O_3 meter.

Research-grade RD587 gasoline with a RON of 92.1 and an octane sensitivity (OS) of 7.3 was used for all tests. Table 2 summarizes the important physical and thermodynamic properties of RD587.

Table 2. RD587 gasoline fuel properties.

Liquid Density @ 15 °C [g/L]	748
LHV [MJ/kg]	41.87
H/C ratio	1.972
O/C ratio	0.033
Research Octane Number	92.1
Octane Sensitivity	7.3
T10 / T50 / T90 [°C]	57 / 98 / 156

A schematic of the engine setup is shown in Figure 2. Pollutant emissions were sampled from the exhaust plenum using heated sampling lines to minimize water and fuel condensation. Dry emissions of carbon monoxide (CO), carbon dioxide (CO_2), and O_2 were measured via a CAI 600 NDIR/Oxygen multi-component analyzer. Unburned hydrocarbon (UHC) emissions were measured by a CAI 600 hydrogen flame ion detector (HFID). Measurements of CO and UHC were used in conjunction with measured injected fuel and air flow rates to calculate combustion efficiency. Nitrogen oxide emissions were measured using a CAI 600 HCLD NO/NOx chemiluminescence analyzer. No measurements of PM were performed in the present study.

For each experiment, the engine was motored for around 30 seconds with the O_3 generator turned on so that uniform and steady O_3 concentrations accumulated in the intake runner. The engine was then fired for 90 seconds with the desired fueling schedule, ST, and O_3 concentration to allow engine surfaces to warm up and emissions measurements to stabilize. For each condition examined, the early and late injection fuel split, ST, and offset between ST and second injection SOI was adjusted iteratively until maximum brake torque (MBT) was achieved provided that ringing intensity (RI) was below 1 MW/m^2 and NOx emissions were below 5 g/kg-fuel. After the 90 seconds warm-up period, 100 cycles worth of data were collected. The engine was then motored, with the entire process repeated for the next operating condition.

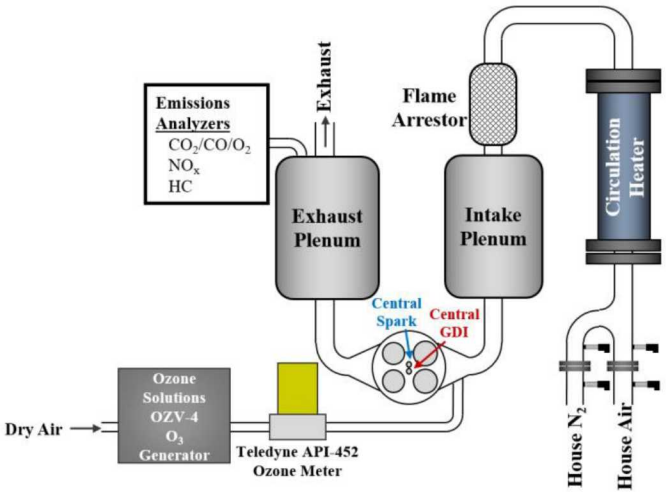

Figure 2. Schematic of the optical engine, gas supply system, O_3 generator, and emissions measurement setup.

Ozone Absorption

Bulk-averaged in-cylinder O_3 concentrations were measured on a CA basis using UV light absorption, as illustrated in Figure 3. Broadband continuous wave light from a Spectra-Physics 250-Watt Xenon arc lamp was partially collimated by a condensing lens and then passed through the combustion chamber via two Nd:YAG 4th harmonic laser line mirrors that selectively reflected only the 266 nm UV light from the lamp. The O_3 absorption cross-section for 266 nm light (σ_{O_3}) is 0.937×10^{-17} cm^2/molecule [33]. A third laser line mirror directed the 266 nm lamp light into an integrating sphere, where the light was detected by a Pacific Instruments 3150RF photomultiplier tube (PMT). The setup minimized the effects of beam steering due to thermal gradients within the combustion chamber.

The in-cylinder O_3 concentration, X_{O_3}, was quantified using three independent datasets that each consisted of 100 ensemble-averaged full-cycle measurements. The "background" dataset was acquired with the lamp light blocked to account for ambient light. The "reference" dataset, I_{ref}, was acquired with the lamp light unblocked and the desired engine fueling schedule performed minus the seeded O_3 to account for light absorption from the ambient gas and any light attenuation from the optical setup. Finally, the "target" dataset, I, was identical to I_{ref} but with O_3 seeding. Only data from the closed portion of the cycle were considered.

Crank angle resolved X_{O_3} was calculated from the partial pressure of O_3, p_{O_3}, that was computed from the Beer-Lambert Law using the following equation:

$$X_{O_3} = \frac{p_{O_3}}{p} = \left(\ln\left[\frac{I_{ref}}{I}\right]\right)\frac{k_B T_{bulk}}{pB\sigma_{O_3}} \quad (1)$$

Here, k_B is the Boltzmann constant $(1.381 \times 10^{-23}\ J/K)$ and B is the cylinder bore diameter. The bulk-gas temperature, T_{bulk}, was estimated from the recorded cylinder pressure assuming isentropic compression. The specific heat ratio at each step was calculated using the mixture composition at IVC and the computed temperature from the previous timestep.

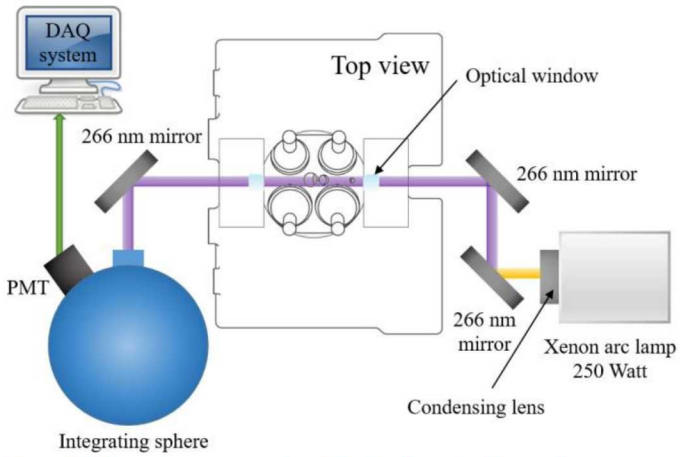

Figure 3. Schematic representation of the O_3 absorption diagnostic.

Note that for fueled conditions, added O_3 can stabilize combustion for the target cycles while misfiring for the associated reference cycles. As a result, high amounts of hot residual CO_2 that absorbs UV light at elevated temperatures [34] are present in the target cycle, but not in the reference cycle. Moreover, hydroperoxyl (HO_2) and hydrogen peroxide (H_2O_2) are prominent combustion intermediates during LTHR and HTHR reactions that likewise absorb UV light [28, 35, 36]. Accordingly, target cycle absorption not from O_3 can differ relative to the reference condition. To combat this effect, the spark was kept inactive so that combustion was suppressed for both the "reference" and "target" cycles. Additionally, intake temperatures were increased such that the range of IVC temperatures achieved matched those from the corresponding fired cycles.

Results and Discussion

The results and discussions section is divided into three subsections. The first subsection describes the impact of O_3 addition on engine performance and emissions characteristics for a range of engine loads (1.5 – 5.5 bar) and speeds (800 – 1600 rpm). Intake pressures and temperatures were fixed at 1.0 bar and 42°C respectively, with intake O_3 concentrations of around 30 ppm. Select results from these conditions are compared to corresponding results from identical conditions minus the intake added O_3. Complementary measurements of crank angle resolved in-cylinder O_3 concentration are used to evaluate the mechanisms of auto-ignition. In the second subsection, the effect of O_3 concentration, ST, early and late injection fuel split, and late injection SOI with respect to ST is described in detail for select operating conditions. Finally, in the third subsection, results from the first two subsections are used to determine the energy required from the deflagration to initiate end gas auto-ignition.

Effect of O_3 addition on engine performance

To highlight the impact of O_3 addition on heat release characteristics, apparent heat release rate (AHRR) profiles are plotted in Figure 4 for a baseline 1000 rpm, 2.8 bar IMEP operating condition with and without 29 ppm of added O_3. The total fueling rate was 11.9 mg/cycle, with 19.9% of the fuel coming in the second injection. The ST was fixed at -54 CA and the second injection SOI occurred 7 CA later. To examine the impact of O_3 decomposition on auto-ignition kinetics, a measured O_3 profile without combustion but had closely matched IVC temperatures to the baseline condition is plotted also in Figure 4.

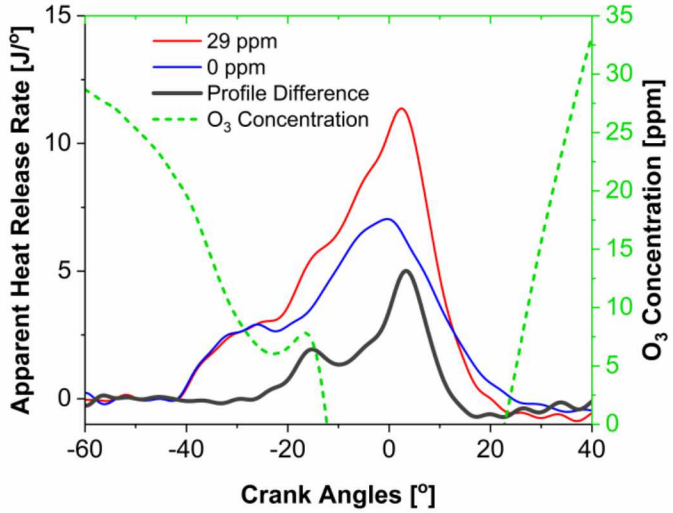

Figure 4. Profiles of AHRR for a 1000 rpm engine speed, 2.8 bar IMEP operating condition with and without 29 ppm of added intake O_3 along with the associated difference between the two profiles. The green dashed profile is the in-cylinder measured O_3 concentration from the absorption experiments.

The first discernable heat release for both profiles occurred around -42 CA, with the AHRR rapidly increasing to an asymptotic value of around 2.6 J/CA by around -32 CA. Until -25 CA, AHRR values for the conditions with and without O_3 addition remained closely matched. The authors speculate that this heat release results from a deflagration that was confined to the piston bowl where rich mixtures from the second injection existed. Beyond this CA, the AHRR slightly dipped for the condition without O_3, possibly due to fuel in this region being completely consumed. However, by -20 CA AHRR values quickly rebounded and reached a peak value of just over 7 J/CA by TDC. It is believed that this larger heat release period results from the slower consumption of leaner end gas mixtures by a deflagration that originates at the piston bowl.

Conversely, the AHRR profile from the condition with O_3 persistently increased beyond the conclusion of the bowl deflagration period, and reached a peak value of almost 12 J/CA by TDC. The sharp increase in AHRR is not consistent with the consumption of lean end gas mixtures by deflagration alone, and suggests that additional heat release occurred due to end gas auto-ignition. To more clearly illustrate the occurrence of end gas auto-ignition, the AHRR profile for the condition without O_3 addition was subtracted from the condition with O_3 addition, and is plotted as the "Profile Difference" in Figure 4. Ozone addition led to a 31% increase in total heat release. Moreover, the profile resembles LTC auto-ignition, with an LTHR period that started around -25 CA and a larger high-temperature heat release (HTHR) period that was centered at TDC. Thermal decomposition of O_3 into O and O_2 started around -60 CA and had nearly concluded by the appearance of LTHR. Secondary absorbance that likewise started around -25 CA was probably from HO_2 formed during LTHR reactions. Because the cool flame combustion would have consumed some amount of fuel that otherwise would have been burned by the deflagration, the overall combustion duration is slightly shorter for the condition without O_3 addition.

Indicated specific fuel consumption (ISFC) and NOx emission index (EI) results are plotted in Figure 5 for a range of engine speeds as a function of engine load. For all conditions, the intake added O_3 concentration was fixed at 30 ppm. These results are compared to

complementary data from a previous study that were acquired from the same engine, but with a homogenous charge at the time of ignition [29]. For the stratified SACI results, ISFC for all engine speeds examined collapsed to a common curve with fuel consumption decreasing by up to 9% relative to nearly identical conditions but without O_3 addition (not shown). The largest declines in ISFC were observed for the lowest engine loads and speeds. Moreover, ISFC data from the previous homogeneous SACI study that had a more limited range of achievable loads and speeds similarly collapsed to the same curve. These results highlight there is no apparent penalty with stratified operation due for example to a change in total heat transfer characteristics.

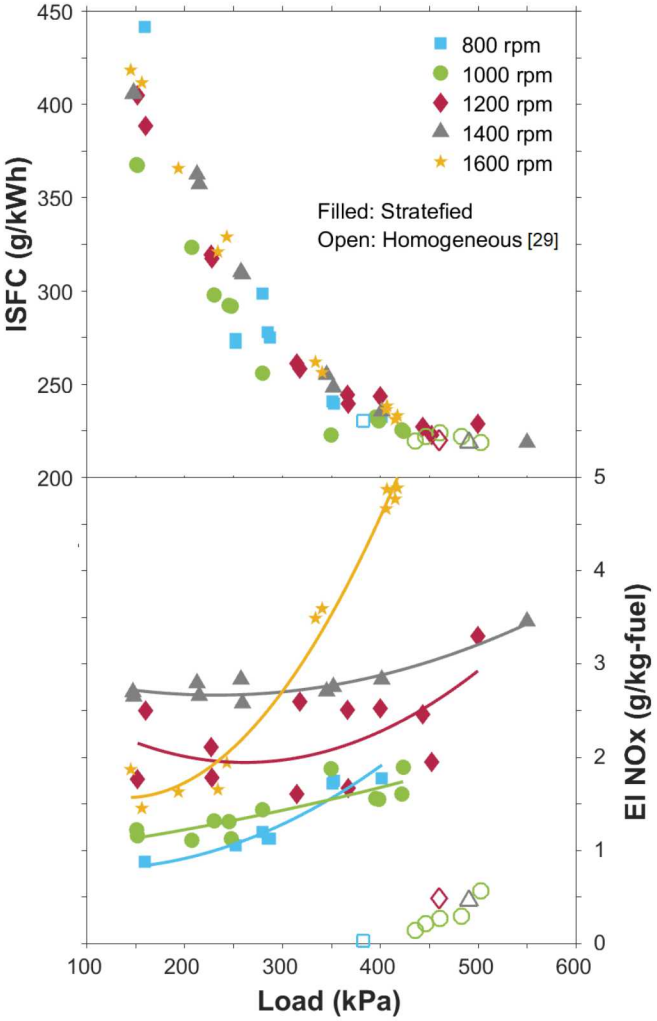

Figure 5. Plots of ISFC and NOx emissions as a function of load at engine speeds of 800 – 1600 rpm for O_3 seeded stratified versus homogeneous SACI. Combustion and emissions characteristics of O_3 added homogenous SACI is discussed in the SAE WCX 2019 paper [29].

For engine speeds of 1400 rpm and lower, NOx emissions had a weak positive correlation with increased engine load and a much stronger positive correlation with increased engine speed. These trends reversed for the load sweep of the highest speed (1600 rpm) condition, which had a much stronger dependence on increased engine load. Homogeneous SACI NOx emissions from our previous study [29] were about an order of magnitude lower than comparable stratified SACI operating points, likely due to the substantial reduction in high-temperature rich regions from the stratified bowl deflagration.

Contour maps of indicated thermal efficiency (ITE), combustion efficiency, coefficient of variation (COV) of IMEP, and 50% burn angle (CA50) are plotted in Figure 6 as a function of engine speed and load for conditions with a fixed 30 ppm amount of added O_3. Note that ST and second injection timing/quantity were adjusted for each operating point until MBT conditions were reached provided that RI values and engine-out NOx emissions remained below 1 MW/m^2 and 5 g/kg-fuel respectfully. It should also be noted that the upper bound on load for all engine speeds was limited by excessive ringing intensities. It is possible that similar benefits could have been achieved if intake O_3 concentrations were reduced from the fixed 30 ppm quantities used here, but such an evaluation was beyond the scope of the present study. Values of ITE varied between 20.0 and 39.6% for the range of operating conditions examined. As expected, increased ITE strongly correlated with an increased load for a given engine speed due to a combination of higher combustion efficiency and more optimal combustion phasing that reduced cycle-to-cycle variability. Increased ITE for a given load was also observed for a decrease in engine speeds that resulted exclusively from higher combustion efficiency. It is thought that longer cycle durations for the slower engine speeds allowed more time for lean mixture combustion to occur.

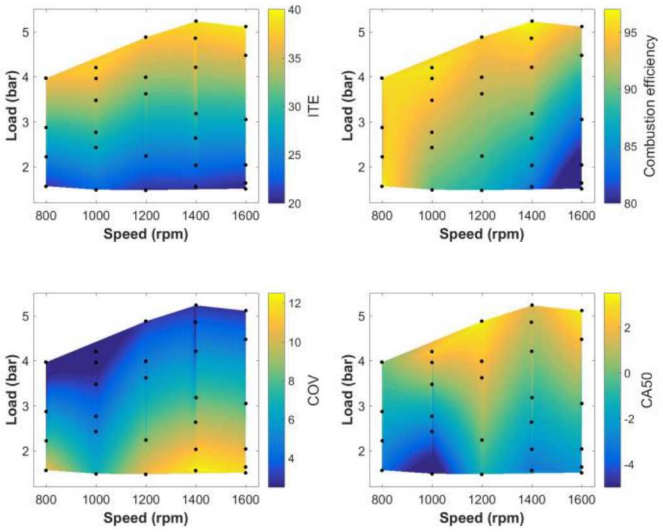

Figure 6. Contour maps of ITE, combustion efficiency, CoV of IMEP, and CA50 for a range of engine speeds (800 – 1600 rpm) and loads (1.5 – 5.5 bar IMEP). Intake O_3 concentration was fixed at 30 ppm (±4 ppm).

Similar contour maps of engine-out NOx, UHC, and CO emissions are plotted in Figure 7. Although the NOx emission threshold was 5 g/kg-fuel, only the highest load and speed conditions evaluated (5+ bar IMEP and 1400+ rpm) actually approached this threshold. Emissions of UHC and CO were generally low for higher loads and lower engine speeds, which is unsurprising given that these are the regions where combustion efficiency was high. As loads decreased and engine speeds increased, UHC emissions steadily climbed. While CO emissions likewise increased with decreased engine load, peak values occurred at lower speeds due to a substantial conversion of hydrocarbons to CO, but the final oxidation step of CO to CO_2 being rate limited.

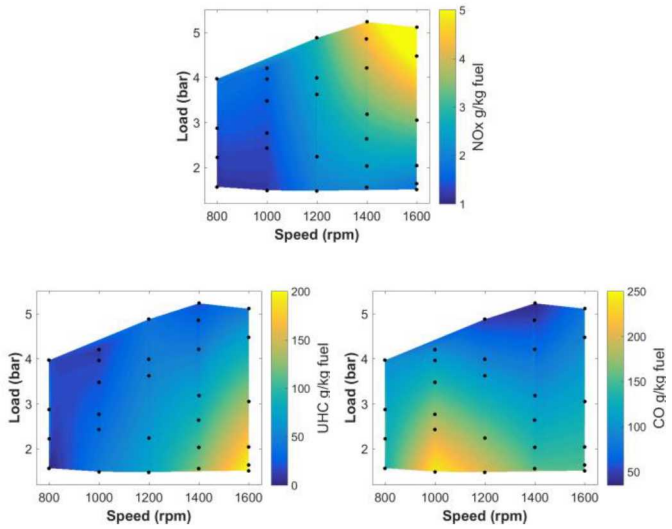

Figure 7. Contour maps of engine-out NOx, UHC, and CO emissions for a range of engine speeds (800 – 1600 rpm) and loads (1.5 – 5.5 bar IMEP). Intake O_3 concentration was fixed at 30 ppm (±4 ppm).

Control variable parametric sweep

Intake O_3 concentration, ST, early and late injection fuel split, and late injection SOI with respect to ST were parametrically varied for select conditions to identify the sensitivity of engine performance and emissions to these parameters. The baseline condition described earlier (1000 rpm, 2.8 bar IMEP) is the first operating point evaluated. Three additional conditions were also evaluated that had similar engine loads (~4 bar IMEP) with varied engine speeds (800, 1200, and 1400 rpm).

Baseline intake O_3 parametric sweep

Figure 4 highlighted the fact that for the baseline condition (1000 rpm, 2.8 bar IMEP), 29 ppm of intake added O_3 promoted the occurrence of end gas auto-ignition by making the charge more reactive. To evaluate the influence of lower O_3 concentrations, additional AHRR profiles for various levels of intake O_3 (0 – 29 ppm) are included for comparison in Figure 8.

Nearly identical AHRR profiles were observed during the early portion of heat release (up to -25 CA). Combustion during this period was believed to be dominated by deflagration of rich bowl mixtures, which suggests that the deflagration was completely unaffected by the small amounts of added O_3. Once again, AHRR profiles for conditions with added O_3 started to diverge around -25 CA relative to the condition without O_3 due to the apparent onset of end gas LTHR reactions. While increased O_3 concentrations led to a greater amount of LTHR, closely matched profiles for the highest O_3 concentrations suggests that the impact began to saturate. It is notable that regardless of the amount of added O_3, LTHR phasing remained closely matched. These results highlight the fact that LTHR onset was driven primarily by the appearance of O produced from thermal decomposition of O_3. The HTHR period was also observed for all conditions that had O_3 addition, with the phasing of this event likewise closely matched for each condition. The magnitude was closely correlated to the amount of LTHR, which itself was tied to the amount of intake O_3.

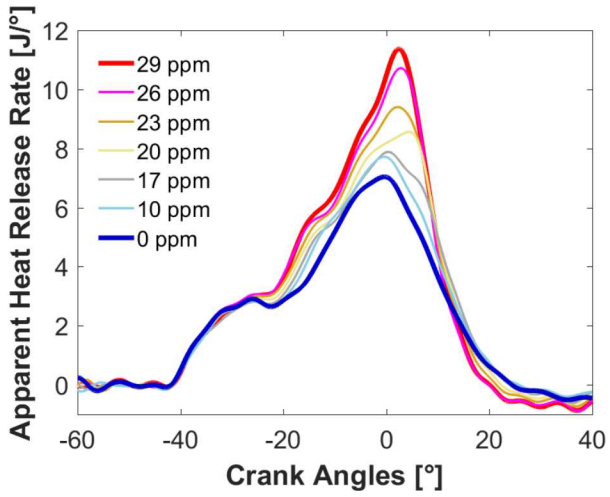

Figure 8. Baseline condition (1000 rpm, 2.8 bar IMEP) AHRR profiles with parametric variations of intake O_3 concentration between 0 and 29 ppm. The profile for the condition with maximum intake O_3 (29 ppm) is plotted in bold red, and the profile with no added O_3 is plotted in bold blue.

Values of ITE, combustion efficiency, COV of IMEP, and engine-out NOx emissions are plotted in Figure 9 for each condition in the baseline O_3 sweep from Figure 8. Figure 9 illustrates that ITE linearly increased with O_3 concentration from 23.5% to 30.7% due mainly to a sharp and persistent drop in COV of IMEP to 5.0%. Engine-out NOx emissions declined 21% as the O_3 concentration was increased from 0 to 29 ppm (i.e., 1.4 to 1.1 g/kg-fuel) as a greater fraction of the fuel combustion was by auto-ignition rather than by deflagration. Finally, it is notable that a decent combustion efficiency of above 95% was achieved regardless of the amount of intake O_3. These results suggest that increased efficiency with increased O_3 addition was not due to better fuel energy conversion, but rather was the result of lower heat transfer and exhaust enthalpy losses.

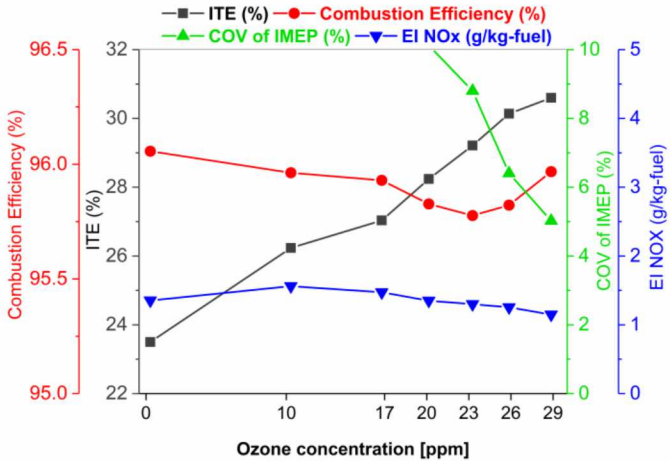

Figure 9. Effect of ozone concentration on ITE, combustion efficiency, COV of IMEP, and NOx emission for the baseline condition (1000 rpm, 2.8 bar IMEP).

Baseline spark timing parametric sweep

Spark timing is an important parameter for stratified SACI with O_3 addition because the resultant deflagration drives the increase in end gas temperatures responsible for thermal decomposition of O_3, and

hence strongly influences the start of LTHR reactions. Profiles of baseline condition AHRR with a fixed 29 ppm intake O_3 concentration and parametric ST sweeps (with a fixed 7 CA offset of the second injection SOI with respect to ST) are plotted in Figure 10. The AHRR profile for the optimal ST (-54 CA) is plotted in bold black, while profiles for ST advance and retard are plotted in blue and magenta respectively.

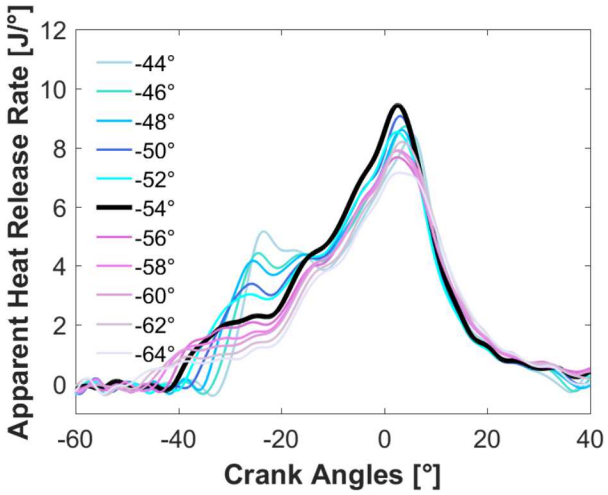

Figure 10. Baseline condition (1000 rpm, 2.8 bar IMEP, 29 ppm of intake O_3) AHRR profiles with parametric variations of ST. The profile from the condition with optimal ST (-54 CA) is plotted in bold black.

When ST was advanced, the start of the initial deflagration period likewise advanced by a comparable amount. Although end gas LTHR and HTHR phasing were unaffected by ST advance, the corresponding deflagration period AHRR was much slower due to slower flame speeds from the lower cylinder temperatures. As a result, integrated deflagration heat release up to the onset of end gas LTHR continuously decreased with ST advance, likely due to increased heat transfer losses from the longer bowl deflagration period. These lower heat release rates persisted throughout the remainder of the cycle. It is unclear from the AHRR profiles alone whether lower end gas deflagration heat release rates were responsible for the decrease in total cycle heat release.

Spark timing retard relative to the optimal condition led to delayed onset of the initial deflagration period with a sharper increase in AHRR due to faster flame speeds. Integrated initial deflagration period heat release up to LTHR onset was roughly comparable to the condition with optimal ST. However, overall heat release rates progressively lowered with ST retard. The apparent reduction in end gas HTHR may be due to a slight dip in AHRR between the LTHR and HTHR periods that grew more prominent with additional ST retard. These AHRR dips may have slowed the increase in end gas temperatures, and thus delayed HTHR onset.

The impact of ST parametric sweeps of values of ITE, combustion efficiency, COV of IMEP, and engine-out NOx emissions are plotted in Figure 11. As with the AHRR profiles from Figure 10, there was a strong discontinuity of emissions and performance trends at the optimal ST. Spark timing retard led to a significant and continuous increase in NOx emissions as the stronger deflagration led to higher flame temperatures. However, ITE declined due to a combination of slightly lower combustion efficiency and less optimally phased end gas HTHR. When ST was advanced, weaker bowl deflagrations sharply decreased combustion stability, which in turn led to a 0.5% drop in combustion efficiency. The combination of lower combustion efficiency, less optimal combustion phasing, and increased heat transfer losses from longer combustion durations led ITE to decrease 2.3 points with only a 2 CA ST retard. Further ST advances led to additional declines in ITE.

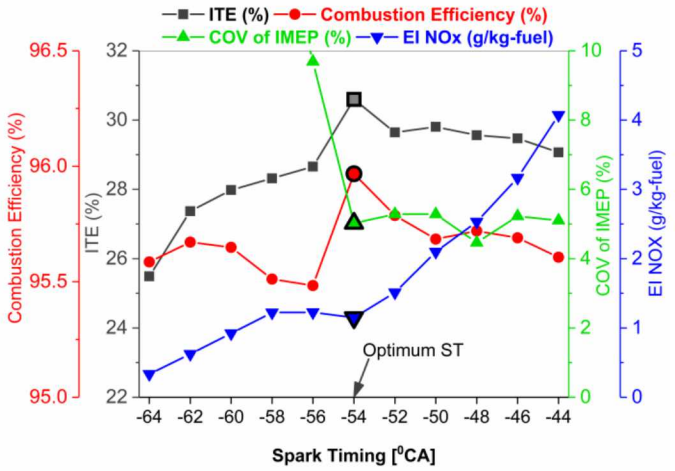

Figure 11. Effect of ST on ITE, combustion efficiency, COV of IMEP, and NOx emission for the baseline condition (1000 rpm, 2.8 bar IMEP, 29 ppm of intake O_3).

Baseline fuel split parametric sweep

The amount of fuel injected during the second injection is an important parameter that determines the strength of the bowl deflagration, and hence the associated amount of end gas heating. Accordingly, parametric sweeps of second injection fueling fraction were performed for the baseline condition to evaluate how this parameter influenced combustion characteristics. For all conditions in the parameter sweep, intake added O_3 and ST were fixed at 30 ppm and -54 CA respectively, with the second injection SOI set 7 CA after ST. Associated AHRR profiles are plotted in Figure 12. The reference optimal condition (19.9% fueling fraction in the second injection) is once again in plotted bold black, with profiles for lower fueling fractions plotted in yellow and higher fueling fractions in red.

For all conditions, the earliest heat release from the bowl mixture deflagration was observed to start at -42 CA. As expected, the strength of this deflagration proportionally increased with the amount of fuel added during the second injection. Evidence of end gas LTHR that started at the conclusion of the early bowl deflagration period was observed for all conditions. Moreover, the end gas LTHR amount and phasing appears to once again have been well-matched across the sweep. Phasing and intensity of the HTHR periods, however, were highly variable. For lower second injection fueling fractions, reduced early deflagration heat release rates led to lower end gas temperatures relative to the optimal condition. As a result, HTHR phasing was sharply advanced with lower peak heat release rates. For higher second injection fueling fractions, the HTHR period was relatively unaffected except for very modest reductions in peak heat release rates likely due to slightly lower end gas fuel fractions.

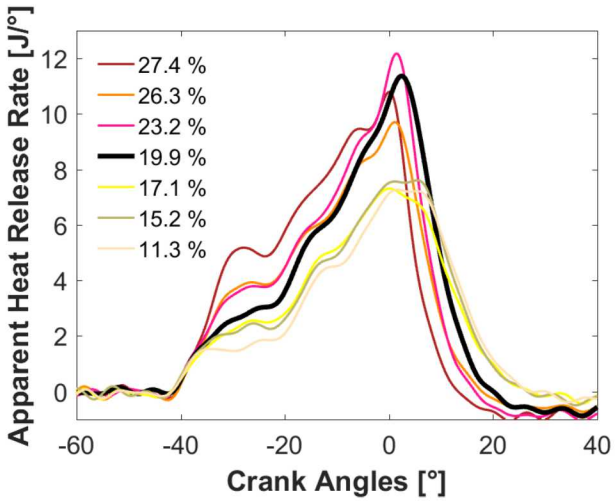

Figure 12. Baseline condition (1000 rpm, 2.8 bar IMEP, 29 ppm of intake O_3) AHRR profiles with parametric variations of second injection fueling fraction. The profile from the condition with optimal second injection fueling fraction (19.9%) is plotted in bold black.

Results of ITE, combustion efficiency, COV of IMEP, and engine-out NOx emissions for the second injection fueling fraction sweep are plotted in Figure 13 to more clearly identify the associated impact on engine performance and emissions. For fueling fractions at or above the optimal value, ITE was consistently above 30% with good combustion efficiency (~96%) and low cycle-to-cycle variability (under 5%). However, NOx emissions exhibited a rapid and non-linear increase with fueling fraction, likely due to increased bowl deflagration temperatures. For lower fueling fractions, the weakness of the initial deflagration period observed in Figure 12 led to a higher amount of cyclic variability that both decreased combustion efficiency and sharply lowered ITE.

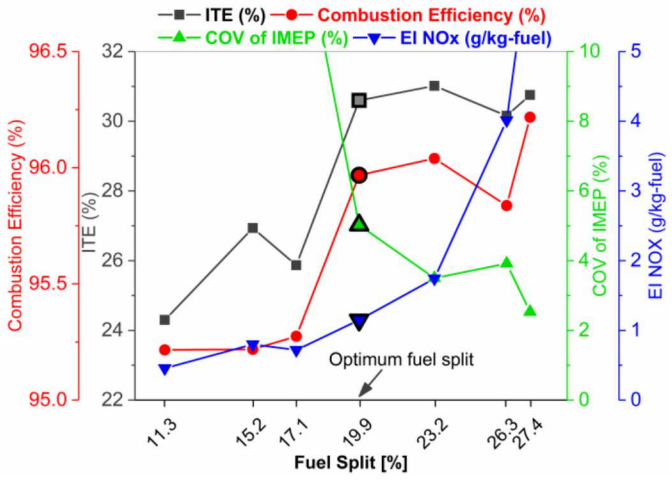

Figure 13. Effect of second injection fueling fraction on ITE, combustion efficiency, COV of IMEP, and NOx emission for the baseline condition (1000 rpm, 2.8 bar IMEP, 29 ppm of intake O_3).

Baseline second injection SOI parametric sweep

The final parameter investigated was the retard in SOI for the second injection relative to a fixed baseline ST (-54 CA). The sweep of second injection SOI retard relative to the ST was varied between 0 (i.e., coincident with ST) and 14 CA. Longer offsets in second injection SOI were expected to increase the amount of fuel spray mixing and bulk-gas entrainment within the bowl, with a higher proportion of premixed combustion. Profiles of AHRR for all conditions in the sweep are plotted in Figure 14. The optimal condition (7 CA offset) is plotted in bold black, with shorter SOI offset values plotted in brown and longer SOI offset values plotted in green.

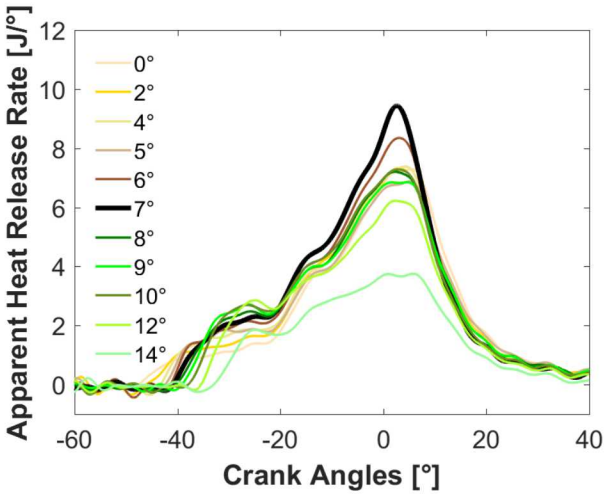

Figure 14. Baseline condition (1000 rpm, 2.8 bar IMEP, 29 ppm of intake O_3) AHRR profiles with parametric variations of second injection SOI retard from the baseline ST (-54 CA). The profile from the condition with optimal second injection SOI retard (7 CA) is plotted in bold black.

From the AHRR profiles in Figure 14, it is evident that a shorter SOI retard led to earlier onset of the deflagration. As with the results from the ST sweeps in Figure 10, the earlier onset led to a weaker overall deflagration period. Once again, end gas LTHR phasing was closely matched for all conditions. Conversely, longer SOI retard led to a stronger deflagration period. It is interesting that SOI offset values retarded beyond the optimal value resulted in a progressive weakening of the end gas LTHR period, with virtually no evidence of LTHR for the largest SOI offset. As a result, HTHR was likewise weaker. It is not clear why this was the case, but it is possible that the delayed deflagration onset led to lower end gas temperatures during O_3 decomposition. As a result, end gas reactions would be much slower.

The impact of second injection SOI retard relative to the ST on ITE, combustion efficiency, COV of IMEP, and NOx emission are plotted in Figure 15. It is immediately evident that the optimal offset hit a very narrow sweet spot with a sharp peak in combustion efficiency and ITE. The weaker deflagration period for shorter SOI offset values and the reduction in LTHR intensity for longer SOI offset values both rapidly increased cyclic variability. As with the other sweeps, the NOx emissions correlated with the amount of AHRR during the initial deflagration period.

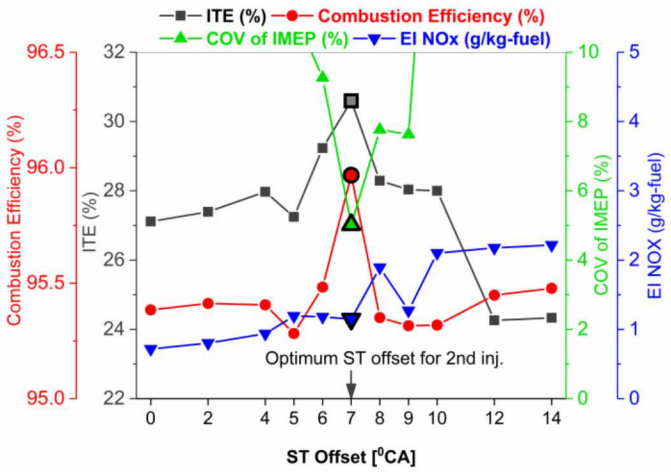

Figure 15. Effect of second injection SOI retard from baseline ST (-54 CA) on ITE, combustion efficiency, COV of IMEP, and NOx emission for the baseline condition (1000 rpm, 2.8 bar IMEP, 29 ppm of intake O_3).

Effect of engine speed for a fixed 4 bar IMEP load

To understand how the baseline condition (1000 rpm, 2.8 bar IMEP) results hold up for higher engine loads and different engine speeds, similar parametric sweeps of intake O_3 concentration were performed for a fixed 4.0 bar IMEP engine load at engine speeds of 800, 1200, and 1400 rpm. Spark timing, second injection SOI retard with respect to ST, and the fuel split between the first and second injections was initially optimized for fixed intake O_3 concentration (~30 ppm) provided that NOx emissions were below 5 g/kg-fuel and RI was below 1 MW/m^2.

Profiles of AHRR for conditions with intake O_3 concentration variations at each engine speed are plotted in Figure 16. Profiles from conditions without intake O_3 are plotted in bold blue, while profiles from conditions with peak intake O_3 are plotted in bold red. For conditions with intermediate concentrations, the profile colors gradually transition between red and blue.

For all engine speeds, AHRR profiles for conditions without intake added O_3 did not exhibit evidence of end gas LTHR. Instead, the same smaller bowl deflagration from the baseline condition was observed, which was followed by a stronger deflagration that consumed end gas mixtures. Each condition did exhibit a secondary increase in heat release rate well after TDC that was likely the result of end gas HTHR reactions. The magnitude of this secondary heat release increased with slower engine speeds, probably due to longer residence times that allowed for more complete oxidation of end gas mixtures.

As intake O_3 concentrations were increased, evidence of end gas LTHR emerged at the conclusion of the initial bowl deflagration period. The magnitude of this heat release increased with O_3 concentration. Moreover, LTHR was most apparent for the lowest 800 rpm engine speed, and steadily weakened as engine speeds increased. Higher intake O_3 concentrations likewise increased end gas HTHR and advanced its phasing. Once again, the magnitude of the increase and amount of phasing advance was greatest for the lowest engine speeds, and steadily waned with higher engine speeds.

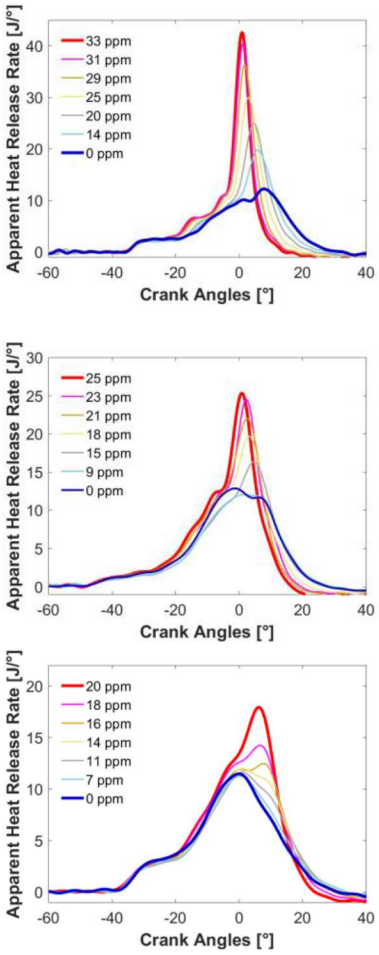

Figure 16. Profiles of AHRR for conditions with a fixed 4 bar IMEP load and engine speeds of (a) 800, (b) 1200, and (c) 1400 rpm. For each engine speed, intake O_3 concentration was varied.

Values of ITE, combustion efficiency, COV of IMEP, CA50, and NOx emissions from each engine speed are plotted in Figure 17 as a function of intake added O_3. For each engine speed condition, ITE substantially increased with increased intake O_3, with peak efficiencies of nearly 40%. Moreover, the effect had not yet saturated, so there is reason to believe that additional increases are possible with larger O_3 concentrations. The improved efficiency was mostly due to an across the board increase in combustion efficiency, decreased cyclic variability, and more optimal combustion phasing that was became centered near TDC. The improved combustion efficiency was most substantial for the higher engine speeds, as the addition of O_3 enabled the HTHR period to fully proceed. Finally, it is notable that for all conditions, NOx emissions remained flat or declined with O_3 addition, which illustrates there is very little downside to the added O_3.

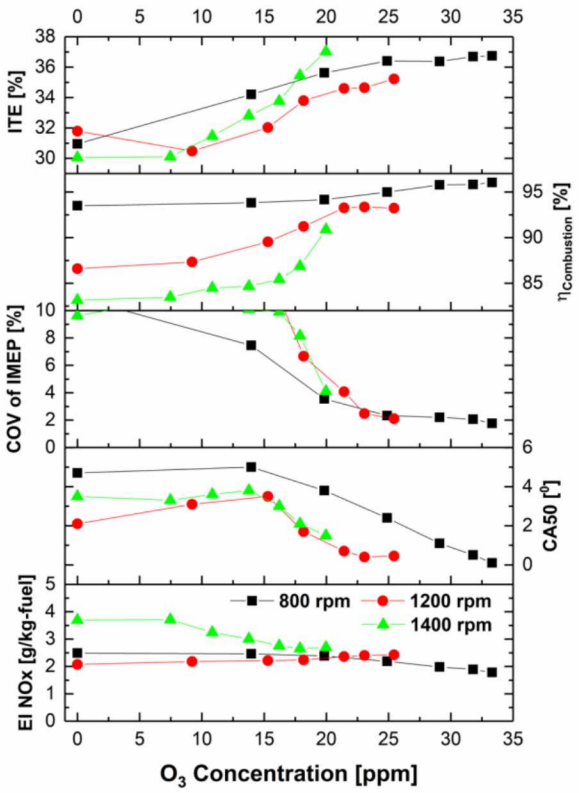

Figure 17. Impact of O_3 concentration sweeps for (a) 800, (b) 1200, and (c) 1400 rpm for a 4 bar IMEP load.

Analysis of the energy requirements for auto-ignition

While end gas reactivity increased with O_3 addition, it was not sufficient on its own to lead to auto-ignition for the fuel-lean conditions examined here. Additional thermal energy supplied by the fuel-rich bowl deflagration was needed to accelerate end gas auto-ignition reactions. However, results from the previous section demonstrated that the second injection was the primary source of NOx emissions. Thus, it is imperative to minimize the second injection fueling fraction while preserving good combustion stability and efficiency for a given condition, which requires new design tools. In the present subsection, a simplified analysis is presented to evaluate the end gas thermal energy deficit needed to initiate sufficiently strong auto-ignition. Optimized conditions used to generate performance and emissions maps in Figures 6 and 7 were used as the reference points.

It was observed earlier that heat release rates from the initial bowl deflagration were well-matched, regardless of the amount of in-cylinder O_3 concentration. Accordingly, the increased thermal energy from the early deflagration can be estimated from the integrated heat release up to the onset of LTHR. The onset of LTHR for each condition was identified from the Profile Difference between the same operating conditions with and without O_3 addition as illustrated in Figure 18. The green hatched area illustrates the integrated energy that is attributed exclusively to the early deflagration heat release.

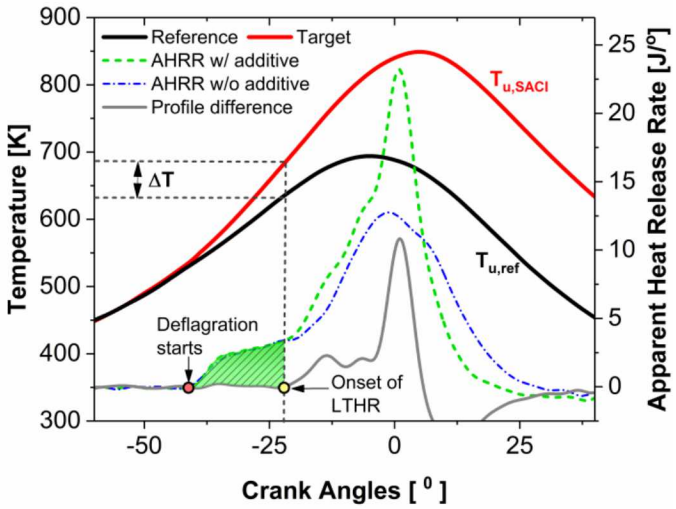

Figure 18. Schematic used to illustrate the methods used to estimate energy added as a result of the bowl deflagration.

A map of the calculated thermal energy deficit required for end gas auto-ignition is plotted in Figure 19 for the full range of load and engine speed conditions evaluated in the present study. The energy deficit varied from 10 Joules for highest load and lowest speed conditions (4 bar IMEP, 800 rpm) to 40 Joules for the lowest loads and highest engine speed conditions (1.5 bar IMEP, 1600 rpm). These results are unsurprising given the longer residence times and more reactive mixtures for the highest load and lowest speed conditions. Indeed, it was often observed that these conditions could sustain auto-ignition without a spark, utilizing only energy addition from retained residual heating. The maps illustrate a fairly linear transition between these two extreme regions.

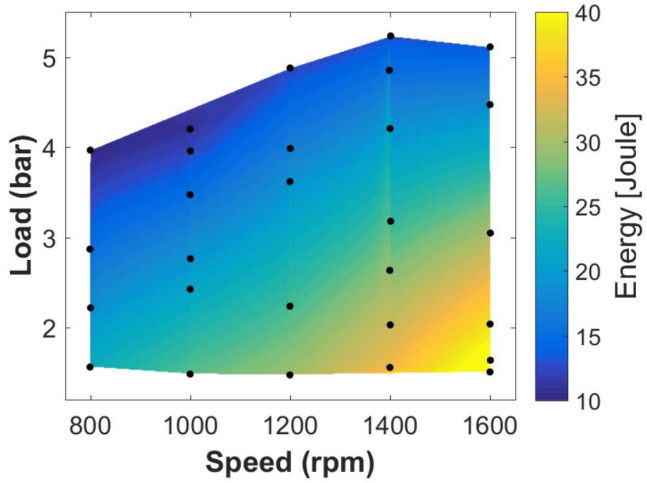

Figure 19. End gas thermal energy deficit estimate from the integrated heat release up to LTHR.

While the integrated heat release provides an estimate for thermal energy addition, it is not very predictive. An alternate method that is potentially more predictive is to evaluate the auto-ignition energy using cycle thermodynamic parameters. For this method, a simple two-zone system was assumed, with deflagration in the piston bowl growing outwardly and end gas mixture getting compressed by this deflagration, as shown in Figure 1. Deflagration and end gas zones

were assumed to be quasi-steady and homogenous, with each zone identified by a single burned or unburned temperature. Thus, the energy required for auto-ignition was the difference in unburned end gas enthalpies for an operating condition relative to a reference motored condition without deflagration. The estimated energy deficit required to initiate end gas auto-ignition can then be written as,

$$E = m_u C_{p,u}(T_{u,SACI} - T_{u,ref}) \quad (2)$$

where m_u is the end gas mass of, $C_{p,u}$ is the end gas constant pressure specific heat, $T_{u,SACI}$ is unburned end gas temperature for stratified SACI condition i.e., with O_3 seeding and the presence of deflagration providing additional energy, and $T_{u,ref}$ is the reference temperature from a corresponding motored condition.

The end gas temperature at the time of LTHR onset was then estimated under the assumption of a polytropic compression. To estimate mixture composition needed to compute the specific heats, the IVC composition was assumed to consist of intake air, fuel from the main injection, and residual gases from the previous cycle. While intake air and fuel masses were measured, the residual gas mass was unknown. To estimate the residual gas mass, the pressure at IVC was divided into partial pressures for intake air, fuel, and residual gas and the ideal gas equation was invoked. The exhaust temperature was used for the residual gases.The resultant estimate for residual gas mass is accordingly as follows:

$$m_r = \frac{R_{exh}T_{exh}}{P_{IVC}V_{IVC}} + \frac{m_{int}R_{int}T_{int} + m_f R_f T_f}{R_{exh}T_{exh}} \quad (3)$$

Subscripts r, int, exh and f, denote residual, intake, exhaust, and fuel respectively. The known composition of the residual gas along with the estimate of residual mass from equation 3 was then used to determine the IVC composition. Temperature at IVC was then solved using the ideal gas equation, the pressure and volume at IVC, and the new estimate for IVC composition. The unburned gas temperature throughout the cycle was then computed at each increment using a polytropic compression with the specific heat ratio updated with the temperature from the previous step calculation. The difference in motored reference and unburned gas temperatures is illustrated in Figure 18.

Unburned gas temperatures at LTHR onset are mapped in Figure 20 for each condition, with values that ranged between 560 and 715 K. The map illustrates that end gas temperature at the onset of auto-ignition increased with engine load, with little dependence on engine speed observed. The result is somewhat surprising given that LTHR onset was primarily driven by O_3 decomposition. However, O_3 decomposition is likely rate limited at the higher engine speeds leading to delayed decomposition. As a result, end gas temperatures were higher by the time that LTHR occurred. A similar argument can be made for the larger bowl deflagrations for the higher load conditions.

A map of calculated end gas thermal energy deficit from Equation 2 is plotted in Figure 21. It is immediately apparent that energy trends for both methods are remarkably well matched. The largest differences between the two methods were observed for the highest load conditions. Relative to the end gas thermal energy deficit calculation that used the integrated heat release, the method that used the difference in end gas temperatures at the onset of LTHR predicts modestly higher values for the lowest engine speeds (2 – 6 J) and modestly lower values (0.5 – 6 J) for the highest speeds. Potential reasons for the discrepancy include: a) errors in the estimated temperature calculation at LTHR onset, b) end gas thermal stratification that would have led to reduced thermal energy requirements for local hot spots, and c) potential fuel stratification from the second injection that likewise would have led locally rich regions that ignite earlier. Future work will evaluate each of these sensitivity parameters in greater detail.

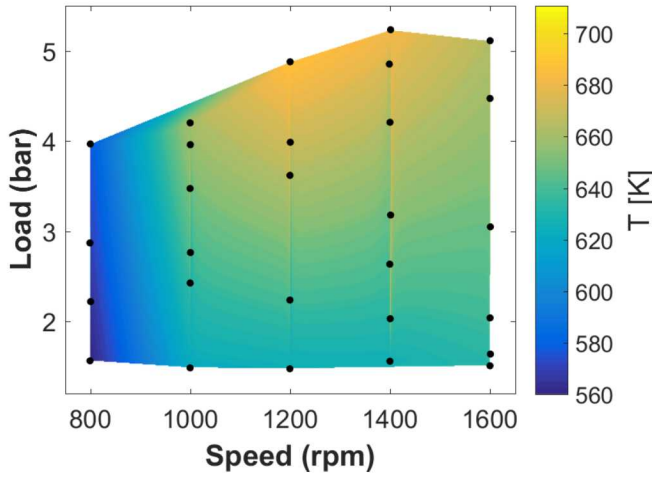

Figure 20. Estimated end gas temperature at the onset of LTHR.

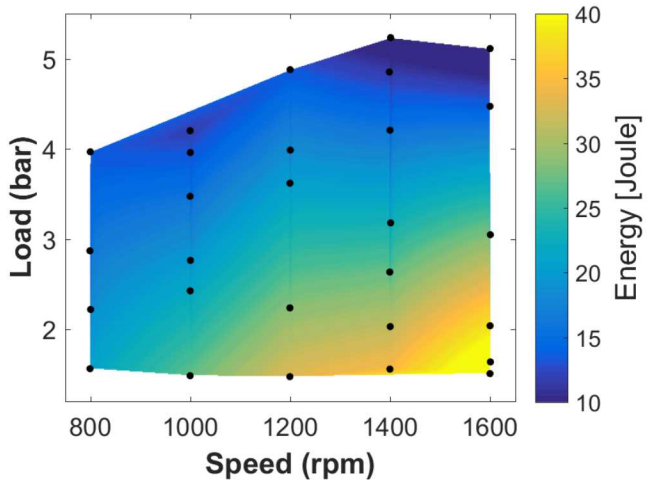

Figure 21. Estimated end gas thermal energy deficit estimate from Equation 2.

Conclusions

In the present study, performance and emissions characteristics were evaluated for stratified lean double injection SACI operation with the addition of the oxidizing agent, O_3 that was seeded into the intake charge. Experiments were performed in an optically accessible single-cylinder research engine with a spray-guided design and 13:1 compression ratio. For all experiments, intake pressure was fixed at 1.0 bar, with a combination of exhaust back-pressure and modest PVO used to produce moderate residuals gas fractions of between 10 and 18%. Engine speeds and loads were varied between 800 – 1600 rpm and 1.5 – 5.5 bar IMEP respectively. Because no external EGR was used, lean charge mixtures (ϕ = 0.27 – 0.56) were produced. For each operating point, the intake O_3 concentration was

fixed at 30 ppm with the fuel split between early and late injections, ST, and second injection SOI retard from ST iteratively adjusted until MBT conditions were achieved provided that cycle RI was below 1 MW/m^2, and NOx emissions were below 5 g/kg-fuel. For select conditions, intake O_3, ST, second injection fueling split, and second injection SOI retard with respect to ST were parametrically varied to better understand the sensitivity of combustion processes to these variables. Performance and emissions results were complemented by quantitative measurements of CA resolved in-cylinder O_3 concentration obtained using a UV absorption diagnostic. Finally, a preliminary analysis was performed to evaluate the optimal amount of thermal energy required to induce lean O_3 containing end gas mixtures to auto-ignite. Major findings are as follows:

- For a given engine load, O_3 addition reduced ISFC for all engine speeds, with the largest reductions of up to 9% occurring for the lowest loads and speeds. Ozone addition also decreased NOx emissions by up to 30%.
- Stratified SACI with O_3 addition featured an initial deflagration of rich piston bowl mixtures that increased end gas temperatures through compressive heating. Simultaneous formation of end gas O by thermal decomposition of the added O_3 led to LTHR onset, which accelerated end gas auto-ignition reactions.
- Increased intake O_3 addition—and hence late-cycle O—led to a corresponding increase in end gas LTHR that accelerated the onset of HTHR. However, the impact of O_3 addition decreased with increased engine speed due to shorter residence times available for auto-ignition.
- Relative to the optimum ST, ST advance slowed deflagration heat release rates, which lowered integrated heat release values at the onset of LTHR and thus delayed HTHR onset. Conversely, stronger early deflagrations with ST retard led to higher flame temperatures that increased NOx emissions.
- Increased fueling fractions in the late second injection likewise increased the strength of the early deflagration, which generally increased combustion stability but led to rapid increases in NOx emissions.
- A simplified thermodynamic analysis method was developed to calculate the energy deficit that used either the integrated heat release up to the onset of LTHR or the difference in end gas temperatures for cycles with and without combustion. Both methods exhibited excellent agreement with each other. For the conditions examined here, roughly 10 to 40 J of thermal energy was needed from the early deflagration to lead to optimized end gas autoignition. Higher speed and lower load conditions required the most energy due to the shorter residence times and leaner end gas mixtures.

The present study demonstrates that the best way to dramatically reduce NOx emissions is to eliminate the late second injection altogether. Ozone addition helps with this by increasing the strength of end gas LTHR reactions and thus requiring a weaker bowl deflagration. While further reductions of second injection fueling fraction are likely possible with even higher O_3 concentrations, this is likely not sufficient to entirely eliminate the second injection. It would be desirable to have the strong deflagration without the second injection, which highlights how the current strategy could be augmented by some form of advanced ignition system (e.g., pre-chamber, low-temperature plasma).

References

1. Kolodziej, C., J. Kodavasal, S. Ciatti, S. Som, N. Shidore, and J. Delhom, "*Achieving Stable Engine Operation of Gasoline Compression Ignition Using 87 AKI Gasoline Down to Idle,*" SAE Technical Paper, 2015. **2015-01-0832**.
2. Pinazzi, P.M. and F. Foucher, "*Potential of Ozone to Enable Low Load Operations of a Gasoline Compression Ignition (GCI) Engine*," in *SAE World Congress Experience*. 2017, SAE International: Detroit, MI.
3. Ciatti, S., M. Johnson, B. Das Adhikary, and R. Reitz, "*Efficiency and Emissions performance of Multizone Stratified Compression Ignition Using Different Octane Fuels,*" SAE World Congress & Exhibition, 2013.
4. Dec, J.E., "*Advanced compression-ignition engines—understanding the in-cylinder processes,*" Proceedings of the Combustion Institute, 2009. **32**(2): p. 2727-2742.
5. Saxena, S. and I.D. Bedoya, "*Fundamental phenomena affecting low temperature combustion and HCCI engines, high load limits and strategies for extending these limits,*" Progress in Energy and Combustion Science, 2013. **39**(5).
6. Fitzgerald, R.P. and R. Steeper, "*Thermal and Chemical Effects of NVO Fuel Injection on HCCI Combustion,*" SAE International Journal of Engines, 2010. **3**(1): p. 46-64.
7. Wolk, B., I. Ekoto, and W. Northrop, "*Investigation of Fuel Effects in Negative Valve Overlap Reforming Chemistry Using Gas Chromatography,*" SAE Int J Engines, 2016. **9**(2).
8. Wolk, B., I. Ekoto, W.F. Northrop, K. Moshammer, and N. Hansen, "*Detailed speciation and reactivity characterization of fuel-specific in-cylinder reforming products and the associated impact on engine performance,*" Fuel, 2016. **185**: p. 348-361.
9. Ekoto, I., B. Wolk, and W. Northrop, "*Energy Analysis of Low-Load Low-Temperature Gasoline Combustion with Auxiliary-Fueled Negative Valve Overlap,*" SAE International Journal of Engines, 2017. **10**(3): p. 1238-1255.
10. Dec, J.E., Y. Yang, J. Dernotte, and C. Ji, "*Effects of Gasoline Reactivity and Ethanol Content on Boosted, Premixed and Partially Stratified Low-Temperature Gasoline Combustion (LTGC),*" SAE Int. J. Engines, 2015. **8**(3).
11. Dernotte, J., J.E. Dec, and C. Ji, "*Energy Distribution Analysis in Boosted HCCI-like / LTGC Engines - Understanding the Trade-Offs to Maximize the Thermal Efficiency,*" SAE Int. J. Engines, 2015. **8**(3).
12. Lawler, B.J. and Z.S. Filipi, "*Integration of a Dual-Mode SI-HCCI Engine Into Various Vehicle Architectures,*" Journal of Engineering for Gas Turbines and Power-Transactions of the Asme, 2013. **135**(5).
13. Manofsky, L., J. Vavra, D.N. Assanis, and A. Babajimopoulos, "*Bridging the Gap between HCCI and SI: Spark-Assisted Compression Ignition*." 2011, SAE International.
14. Persson, H., A. Hultqvist, B. Johansson, and A. Remón, "*Investigation of the Early Flame Development in Spark Assisted HCCI Combustion Using High Speed Chemiluminescence Imaging*." 2007, SAE International.
15. Reuss, D.L., Kuo, T.-W., Silvas, G., Natarajan, V., Sick, V., "*Experimental metrics for identifying origins of combustion variability during spark-assisted compression ignition,*" International Journal of Engine Research, 2008. **9**(5): p. 409-434.

16. Lavoie, G.A., J. Martz, M. Wooldridge, and D. Assanis, "*A multi-mode combustion diagram for spark assisted compression ignition,*" Combustion and Flame, 2010. **157**(6): p. 1106-1110.
17. Benajes, J., A. García, V. Domenech, and R. Durrett, "*An investigation of partially premixed compression ignition combustion using gasoline and spark assistance,*" Applied Thermal Engineering, 2013. **52**(2): p. 468-477.
18. Benajes, J., S. Molina, A. García, J. Monsalve-Serrano, and R. Durrett, "*Performance and engine-out emissions evaluation of the double injection strategy applied to the gasoline partially premixed compression ignition spark assisted combustion concept,*" Applied Energy, 2014. **134**: p. 90-101.
19. Olesky, L.M., J.B. Martz, G.A. Lavoie, J. Vavra, D.N. Assanis, and A. Babajimopoulos, "*The effects of spark timing, unburned gas temperature, and negative valve overlap on the rates of stoichiometric spark assisted compression ignition combustion,*" Applied Energy, 2013. **105**: p. 407-417.
20. Olesky, L.M., G.A. Lavoie, D.N. Assanis, M.S. Wooldridge, and J.B. Martz, "*The effects of diluent composition on the rates of HCCI and spark assisted compression ignition combustion,*" Applied Energy, 2014. **124**: p. 186-198.
21. Ortiz-Soto, E.A., G.A. Lavoie, J.B. Martz, M.S. Wooldridge, and D.N. Assanis, "*Enhanced heat release analysis for advanced multi-mode combustion engine experiments,*" Applied Energy, 2014. **136**: p. 465-479.
22. Middleton, R.J., L.K.M. Olesky, G.A. Lavoie, M.S. Wooldridge, D.N. Assanis, and J.B. Martz, "*The effect of spark timing and negative valve overlap on Spark Assisted Compression Ignition combustion heat release rate,*" Proceedings of the Combustion Institute, 2015. **35**(3): p. 3117-3124.
23. Olesky, L.K.M., R.J. Middleton, G.A. Lavoie, M.S. Wooldridge, and J.B. Martz, "*On the sensitivity of low temperature combustion to spark assist near flame limit conditions,*" Fuel, 2015. **158**: p. 11-22.
24. Masurier, J.B., F. Foucher, G. Dayma, and P. Dagaut, "*Ozone applied to the homogeneous charge compression ignition engine to control alcohol fuels combustion,*" Applied Energy, 2015. **160**(Supplement C): p. 566-580.
25. Masurier, J.-B., F. Foucher, G. Dayma, and P. Dagaut, "*Investigation of iso-octane combustion in a homogeneous charge compression ignition engine seeded by ozone, nitric oxide and nitrogen dioxide,*" Proceedings of the Combustion Institute, 2015. **35**(3): p. 3125-3132.
26. Masurier, J.B., F. Foucher, G. Dayma, and P. Dagaut, "*Homogeneous Charge Compression Ignition Combustion of Primary Reference Fuels Influenced by Ozone Addition,*" Energy & Fuels, 2013. **27**(9): p. 5495-5505.
27. Truedsson, I., C. Rousselle, and F. Foucher, "*Ozone Seeding Effect on the Ignition Event in HCCI Combustion of Gasoline-Ethanol Blends*," in *SAE World Congress Experience*. 2017, SAE International: Detroit, MI.
28. Ekoto, I. and F. Foucher, "*Mechanisms of Enhanced Reactivity with Ozone Addition for Advanced Compression Ignition*," in *SAE World Congress Experience*. 2018, SAE International: Detroit, MI.
29. Biswas, S. and I. Ekoto, "*Detailed Investigation into the Effect of Ozone Addition on Spark Assisted Compression Ignition Engine Performance and Emissions Characteristics,*" SAE Technical Paper 2019-01-0966, 2019.
30. Shiraishi, T., "*Possibility of the new Ignition System using the low Temperature Plasma having dual Function of strengthening Ignition for SI Combustion and promoting and controlling Autoignition of HCCI Combustion,*" Advanced Ignition Systems for Gasoline Engines, eds. Kratzsch M, Günther M; Renningen, Germany: expert verlag 2013: p. 82-94.
31. Smekhov, G.D., L.B. Ibraguimova, S.P. Karkach, O.V. Skrebkov, and O.P. Shatalov, "*Numerical simulation of ignition of a hydrogen-oxygen mixture in view of electronically excited components,*" High Temperature, 2007. **45**(3): p. 395-407.
32. Zádor, J., C.A. Taatjes, and R.X. Fernandes, "*Kinetics of elementary reactions in low-temperature autoignition chemistry,*" Progress in Energy and Combustion Science, 2011. **37**(4): p. 371-421.
33. Gorshelev, V., A. Serdyuchenko, M. Weber, W. Chehade, and J.P. Burrows, "*High spectral resolution ozone absorption cross-sections - Part 1: Measurements, data analysis and comparison with previous measurements around 293 K,*" Atmospheric Measurement Techniques, 2014. **7**(2): p. 609-624.
34. Schulz, C., J.D. Koch, D.F. Davidson, J.B. Jeffries, and R.K. Hanson, "*Ultraviolet absorption spectra of shock-heated carbon dioxide and water between 900 and 3050 K,*" Chemical Physics Letters, 2002. **355**(1-2): p. 82-88.
35. Kijewski, H. and J. Troe, "*Study of the pyrolysis of H2O2 in the presence of H2and CO by use of UV absorption of HO2,*" International Journal of Chemical Kinetics, 1971. **3**(3): p. 223-235.
36. Molina, L.T. and M.J. Molina, "*UV Absorption Cross-Sections of HO2NO2 Vapor,*" Journal of Photochemistry, 1981. **15**(2): p. 97-108.

Contact Information

Isaac Wesley Ekoto
iekoto@sandia.gov
Sandia National Laboratories
P.O. Box 969, MS 9053
Livermore, CA 94551, USA

Acknowledgments

The authors would like to thank Alberto Garcia, Gary Hubbard, and Keith Penney for their dedicated support of the Gasoline Combustion Fundamentals Laboratory. The work was performed at the Combustion Research Facility, Sandia National Laboratories, Livermore, CA. Financial support was provided by the U.S. Department of Energy, Vehicle Technologies Office. Sandia National Laboratories is a multi-mission laboratory managed and operated by National Technology and Engineering Solutions of Sandia, LLC., a wholly owned subsidiary of Honeywell International, Inc., for the U.S. Department of Energy's National Nuclear Security Administration under contract DE-NA0003525.

Definitions/Abbreviations

ϕ	equivalence ratio
ϕ'	Charge mass equivalence ratio
σ_{O_3}	Ozone absorption cross-section

ACI	Advanced compression ignition
AHRR	Apparent heat release rate
B	Bore diameter [m]
CA	Crank angle referenced to main TDC [°]
CA50	50% cumulative burn angle
CO	Carbon monoxide
CO_2	Carbon dioxide
CoV	Coefficient of variation
C_p	Constant pressure specific heat [J/kg-K]
DI	Direct injection
E	Energy [J]
EGR	Exhaust gas recirculation
EVC/EVO	Exhaust valve close/open
DI	Direct injection
H/C	Hydrogen-to-carbon ratio
H_2O	Water
HO_2	Hydroperoxyl
H_2O_2	Hydrogen peroxide
HC	Hydrocarbon
HTHR	High-temperature heat release
I_{ref}	Reference intensity
IMEP	Indicated mean effective pressure
ITE	Indicated thermal efficiency
ITHR	Intermediate-temperature heat release
IVC/IVO	Intake valve close/open
LHV	Lower heating value [kJ/g]
LTHR	Low-temperature heat release
m	Mass [kg]
MBT	Maximum brake torque
N_2	Nitrogen
NO	Nitric oxide
NO_2	Nitrogen dioxide
NOx	Nitrogen oxide
NVO	Negative valve overlap
O	Atomic oxygen
O_2	Molecular oxygen
O_3	Ozone
OH	Hydroxyl
OS	Octane sensitivity
P	Pressure [Pa]
PID	Proportional, Integral, Derivative
PM	Particulate matter
PMT	Photomultiplier tube
ppm	Parts per million
PVO	Positive valve overlap
R	Alkyl radical
R	Gas constant [J/kg-K]
RI	Ringing intensity [Mw/m^2]
ROOH	Alkylhydroperoxide
RON	Research octane number
rpm	Revolutions per minute
SACI	Spark assisted compression ignition
SI	Spark ignition
SOI	Start of fuel injection
ST	Spark timing
T	Temperature [K]
T10/T50/T90	10%, 50%, and 90% boiling points
TDC	Top dead center
UV	Ultraviolet

Subscripts

$1, 2$	First injection, second injection
b	Burned
$bulk$	Bulk/Averaged
exh	Exhaust
f	Fuel
int	Intake
r	Residual
ref	Reference
u	Unburned